

We are IntechOpen, the world's leading publisher of Open Access books Built by scientists, for scientists

6,900

Open access books available

186,000

International authors and editors

200M

Downloads

Our authors are among the

154

Countries delivered to

TOP 1%

most cited scientists

12.2%

Contributors from top 500 universities



WEB OF SCIENCE™

Selection of our books indexed in the Book Citation Index
in Web of Science™ Core Collection (BKCI)

Interested in publishing with us?
Contact book.department@intechopen.com

Numbers displayed above are based on latest data collected.
For more information visit www.intechopen.com



Aerodynamic Heating at Hypersonic Speed

Andrey B. Gorshkov
*Central Research Institute of Machine Building
Russia*

1. Introduction

At designing and modernization of a reentry space vehicle it is required accurate and reliable data on the flow field, aerodynamic characteristics, heat transfer processes. Taking into account the wide range of flow conditions, realized at hypersonic flight of the vehicle in the atmosphere, it leads to the need to incorporate in employed theoretical models the effects of rarefaction, viscous-inviscid interaction, flow separation, laminar-turbulent transition and a variety of physical and chemical processes occurring in the gas phase and on the vehicle surface.

Getting the necessary information through laboratory and flight experiments requires considerable expenses. In addition, the reproduction of hypersonic flight conditions at ground experimental facilities is in many cases impossible. As a result the theoretical simulation of hypersonic flow past a spacecraft is of great importance. Use of numerical calculations with their relatively small cost provides with highly informative flow data and gives an opportunity to reproduce a wide range of flow conditions, including the conditions that cannot be reached in ground experimental facilities. Thus numerical simulation provides the transfer of experimental data obtained in laboratory tests on the flight conditions.

One of the main problems that arise at designing a spacecraft reentering the Earth's atmosphere with orbital velocity is the precise definition of high convective heat fluxes (aerodynamic heating) to the vehicle surface at hypersonic flight. In a dense atmosphere, where the assumption of continuity of gas medium is true, a detailed analysis of parameters of flow and heat transfer of a reentry vehicle may be made on the basis of numerical integration of the Navier-Stokes equations allowing for the physical and chemical processes in the shock layer at hypersonic flight conditions. Taking into account the increasing complexity of practical problems, a task of verification of employed physical models and numerical techniques arises by means of comparison of computed results with experimental data.

In this chapter some results are presented of calculations of perfect gas and real air flow, which have been obtained using a computer code developed by the author (Gorshkov, 1997). The code solves two- or three-dimensional Navier-Stokes equations cast in conservative form in arbitrary curvilinear coordinate system using the implicit iteration scheme (Yoon & Jameson, 1987). Three gas models have been used in the calculations: perfect gas, equilibrium and nonequilibrium chemically reacting air. Flow is supposed to be laminar.

The first two cases considered are hypersonic flow of a perfect gas at wind tunnel conditions. In experiments conducted at the Central Research Institute of Machine Building

(TsNIImash) (Gubanova et al, 1992), areas of elevated heat fluxes have been found on the windward side of a delta wing with blunt edges. Here results of computations are presented which have been made to numerically reproduce the observed experimental effect.

The second case is hypersonic flow over a test model of the Pre-X demonstrator (Baiocco et al., 2006), designed to glide in the Earth's atmosphere. A comparison between thermovision experimental data on heat flux obtained in TsNIImash and calculation results is made.

As the third case a flow of dissociating air at equilibrium and nonequilibrium conditions is considered. The characteristics of flow field and convective heat transfer are presented over a winged configuration of a small-scale reentry vehicle (Vaganov et al, 2006), which was developed in Russia, at some points of a reentry trajectory in the Earth's atmosphere.

2. Basic equations

For the three-dimensional flows of a chemically reacting nonequilibrium gas mixture in an arbitrary curvilinear coordinate system:

$$\xi = \xi(x, y, z, t), \quad \eta = \eta(x, y, z, t), \quad \zeta = \zeta(x, y, z, t), \quad \tau = t$$

the Navier-Stokes equations in conservative form can be written as follows (see eg. Hoffmann & Chiang, 2000):

$$\frac{\partial \mathbf{Q}}{\partial \tau} + \frac{\partial \mathbf{E}}{\partial \xi} + \frac{\partial \mathbf{F}}{\partial \eta} + \frac{\partial \mathbf{G}}{\partial \zeta} = \mathbf{S} \quad (1)$$

$$J^{-1} = \partial(x, y, z) / \partial(\xi, \eta, \zeta), \quad \mathbf{E} = J^{-1}(\xi_t \mathbf{Q} + \xi_x \mathbf{E}_c + \xi_y \mathbf{F}_c + \xi_z \mathbf{G}_c),$$

$$\mathbf{F} = J^{-1}(\eta_t \mathbf{Q} + \eta_x \mathbf{E}_c + \eta_y \mathbf{F}_c + \eta_z \mathbf{G}_c), \quad \mathbf{G} = J^{-1}(\zeta_t \mathbf{Q} + \zeta_x \mathbf{E}_c + \zeta_y \mathbf{F}_c + \zeta_z \mathbf{G}_c)$$

Here J - Jacobian of the coordinate transformation, and metric derivatives are related by:

$$\xi_x = J(y_\eta z_\zeta - y_\zeta z_\eta), \quad \xi_t = -x_\tau \xi_x - y_\tau \xi_y - z_\tau \xi_z, \text{ etc.}$$

\mathbf{Q} is a vector of the conservative variables, \mathbf{E}_c , \mathbf{F}_c and \mathbf{G}_c are x , y and z components of mass, momentum and energy in Cartesian coordinate system, \mathbf{S} is a source term taking into account chemical processes:

$$\mathbf{Q} = \begin{pmatrix} \rho \\ \rho u \\ \rho v \\ \rho w \\ e \\ \rho_i \end{pmatrix}; \quad \mathbf{E}_c = \begin{pmatrix} \rho u \\ \rho u^2 + p - \tau_{xx} \\ \rho uv - \tau_{xy} \\ \rho uw - \tau_{xz} \\ (e + p)u - m_x \\ \rho_i u + d_{i,x} \end{pmatrix}; \quad \mathbf{F}_c = \begin{pmatrix} \rho v \\ \rho vu - \tau_{xy} \\ \rho v^2 + p - \tau_{yy} \\ \rho vw - \tau_{yz} \\ (e + p)v - m_y \\ \rho_i v + d_{i,y} \end{pmatrix}; \quad \mathbf{G}_c = \begin{pmatrix} \rho w \\ \rho wu - \tau_{xz} \\ \rho wv - \tau_{yz} \\ \rho w^2 + p - \tau_{zz} \\ (e + p)w - m_z \\ \rho_i w + d_{i,z} \end{pmatrix}; \quad \mathbf{S} = \begin{pmatrix} 0 \\ 0 \\ 0 \\ 0 \\ 0 \\ \omega_i \end{pmatrix}$$

$$m_x = u \tau_{xx} + v \tau_{xy} + w \tau_{xz} - q_x; \quad m_y = u \tau_{xy} + v \tau_{yy} + w \tau_{yz} - q_y; \quad m_z = u \tau_{xz} + v \tau_{yz} + w \tau_{zz} - q_z$$

where ρ , ρ_i - densities of the gas mixture and chemical species i ; u , v and w - Cartesian velocity components along the axes x , y and z respectively; the total energy of the gas mixture per unit volume e is the sum of internal ε and kinetic energies:

$$e = \rho\varepsilon + \rho(u^2 + v^2 + w^2) / 2$$

The components of the viscous stress tensor are:

$$\begin{aligned} \tau_{xx} &= 2\mu \frac{\partial u}{\partial x} + \lambda \operatorname{div} \mathbf{V}, & \tau_{yy} &= 2\mu \frac{\partial v}{\partial y} + \lambda \operatorname{div} \mathbf{V}, & \tau_{zz} &= 2\mu \frac{\partial w}{\partial z} + \lambda \operatorname{div} \mathbf{V} \\ \tau_{xy} &= \mu \left(\frac{\partial u}{\partial y} + \frac{\partial v}{\partial x} \right), & \tau_{xz} &= \mu \left(\frac{\partial u}{\partial z} + \frac{\partial w}{\partial x} \right), & \tau_{yz} &= \mu \left(\frac{\partial v}{\partial z} + \frac{\partial w}{\partial y} \right), & \operatorname{div} \mathbf{V} &= \frac{\partial u}{\partial x} + \frac{\partial v}{\partial y} + \frac{\partial w}{\partial z} \end{aligned}$$

Inviscid parts of the fluxes $\mathbf{E} = \mathbf{E}_{inv} - \mathbf{E}_v$, $\mathbf{F} = \mathbf{F}_{inv} - \mathbf{F}_v$ и $\mathbf{G} = \mathbf{G}_{inv} - \mathbf{G}_v$ in a curvilinear coordinate system have the form:

$$\mathbf{E}_{inv} = J^{-1} \begin{pmatrix} \rho U \\ \rho U u + \xi_x p \\ \rho U v + \xi_y p \\ \rho U w + \xi_z p \\ (e+p)U - \xi_t p \\ \rho_t U \end{pmatrix}; \quad \mathbf{F}_{inv} = J^{-1} \begin{pmatrix} \rho V \\ \rho V u + \eta_x p \\ \rho V v + \eta_y p \\ \rho V w + \eta_z p \\ (e+p)V - \eta_t p \\ \rho_i V \end{pmatrix}; \quad \mathbf{G}_{inv} = J^{-1} \begin{pmatrix} \rho W \\ \rho W u + \zeta_x p \\ \rho W v + \zeta_y p \\ \rho W w + \zeta_z p \\ (e+p)W - \zeta_t p \\ \rho_i W \end{pmatrix}$$

where U , V and W - velocity components in the transformed coordinate system:

$$U = \xi_t + \xi_x u + \xi_y v + \xi_z w, \quad V = \eta_t + \eta_x u + \eta_y v + \eta_z w, \quad W = \zeta_t + \zeta_x u + \zeta_y v + \zeta_z w$$

Fluxes due to processes of molecular transport (viscosity, diffusion and thermal conductivity) \mathbf{E}_v , \mathbf{F}_v и \mathbf{G}_v in a curvilinear coordinate system

$$\mathbf{E}_v = J^{-1} \begin{pmatrix} 0 \\ \xi_x \tau_{xx} + \xi_y \tau_{xy} + \xi_z \tau_{xz} \\ \xi_x \tau_{xy} + \xi_y \tau_{yy} + \xi_z \tau_{yz} \\ \xi_x \tau_{xz} + \xi_y \tau_{yz} + \xi_z \tau_{zz} \\ \xi_x m_x + \xi_y m_y + \xi_z m_z \\ -(\xi_x d_{i,x} + \xi_y d_{i,y} + \xi_z d_{i,z}) \end{pmatrix}; \quad \mathbf{F}_v = J^{-1} \begin{pmatrix} 0 \\ \eta_x \tau_{xx} + \eta_y \tau_{xy} + \eta_z \tau_{xz} \\ \eta_x \tau_{xy} + \eta_y \tau_{yy} + \eta_z \tau_{yz} \\ \eta_x \tau_{xz} + \eta_y \tau_{yz} + \eta_z \tau_{zz} \\ \eta_x m_x + \eta_y m_y + \eta_z m_z \\ -(\eta_x d_{i,x} + \eta_y d_{i,y} + \eta_z d_{i,z}) \end{pmatrix}$$

$$\mathbf{G}_v = J^{-1} \begin{pmatrix} 0 \\ \zeta_x \tau_{xx} + \zeta_y \tau_{xy} + \zeta_z \tau_{xz} \\ \zeta_x \tau_{xy} + \zeta_y \tau_{yy} + \zeta_z \tau_{yz} \\ \zeta_x \tau_{xz} + \zeta_y \tau_{yz} + \zeta_z \tau_{zz} \\ \zeta_x m_x + \zeta_y m_y + \zeta_z m_z \\ -(\zeta_x d_{i,x} + \zeta_y d_{i,y} + \zeta_z d_{i,z}) \end{pmatrix}$$

Partial derivatives with respect to x , y and z in the components of the viscous stress tensor and in flux terms, describing diffusion $\mathbf{d}_i = (d_{ix}, d_{iy}, d_{iz})$ and thermal conductivity $\mathbf{q} = (q_x, q_y, q_z)$, are calculated according to the chain rule.

2.1 Chemically reacting nonequilibrium air

In the calculation results presented in this chapter air is assumed to consist of five chemical species: N_2 , O_2 , NO , N , O . Vibrational and rotational temperatures of molecules are equal to the translational temperature. Pressure is calculated according to Dalton's law for a mixture of ideal gases:

$$p = \frac{\rho RT}{M_{gm}} = \sum p_i = \sum \frac{\rho_i RT}{M_i}$$

where M_{gm} , M_i - molecular weights of the gas mixture and the i -th chemical species. The internal energy of the gas mixture per unit mass is:

$$\varepsilon = \sum_i c_i h_{fi} + \sum_i c_i C_{vi} T + \sum_i c_i \varepsilon_{ei}(T) + \sum_m c_i \varepsilon_{vm}(T)$$

Here $c_i = \rho_i / \rho$, h_{fi} , ε_{ei} - mass concentration, formation enthalpy and energy of electronic excitation of species i , C_{vi} - heat capacity at constant volume of the translational and rotational degrees of freedom of species i , equal to $3/2(R/M_i)$ for atoms and $5/2(R/M_i)$ for diatomic molecules. Vibrational energy ε_{vm} of the m -th molecular species is calculated in the approximation of the harmonic oscillator. The diffusion fluxes of the i -th chemical species are determined according to Fick's law and, for example, in the direction of the x -axis have the form:

$$d_{i,x} = -\rho D_i \frac{\partial c_i}{\partial x}$$

To determine diffusion coefficients D_i approximation of constant Schmidt numbers $Sc_i = \mu / \rho D_i$ is used, which are supposed to be equal to 0.75 for atoms and molecules. Total heat flux \mathbf{q} is the sum of heat fluxes by thermal conductivity and diffusion of chemical species:

$$q_x = -\kappa \frac{\partial T}{\partial x} + \sum_i h_i d_{i,x}; \quad h_i = C_{pi} T + \varepsilon_{vi}(T) + \varepsilon_{ei}(T) + h_{fi}$$

where h_i , C_{pi} - enthalpy and heat capacity at constant pressure of translational and rotational degrees of freedom of the i -th chemical species per unit mass. Viscosity μ and thermal conductivity κ of nonequilibrium mixture of gases are found by formulas of Wilke (1950) and of Mason & Saxena (1958).

The values of the rate constants of chemical reactions were taken from (Vlasov et al., 1997) where they were selected on the basis of various theoretical and experimental data, in particular, as a result of comparison with flight data on electron density in the shock layer near the experimental vehicle RAM-C (Grantham, 1970). Later this model of nonequilibrium air was tested in (Vlasov & Gorshkov, 2001) for conditions of hypersonic flow past the reentry vehicle OREX (Inouye, 1995).

2.2 Perfect gas and equilibrium air

In the calculations using the models of perfect gas and equilibrium air mass conservation equations of chemical species in the system (1) are absent. For a perfect gas the viscosity is determined by Sutherland's formula, thermal conductivity is found from the assumption of the constant Prandtl number $Pr = 0.72$. For equilibrium air pressure, internal energy, viscosity and thermal conductivity are determined from the thermodynamic relations:

$$p = p(\rho, T); \quad \varepsilon = \varepsilon(\rho, T); \quad \mu = \mu(\rho, T); \quad \kappa = \kappa(\rho, T)$$

2.3 Boundary conditions

On the body surface a no-slip condition of the flow $u = v = w = 0$, fixed wall temperature $T_w = \text{const}$ or adiabatic wall $q_w = \varepsilon_w \sigma T_w^4$ are specified, where q_w - total heat flux to the surface due to heat conduction and diffusion of chemical species (2), $\varepsilon_w = 0.8$ - emissivity of thermal protection material, σ - Stefan-Boltzmann's constant.

Concentrations of chemical species on the surface are found from equations of mass balance, which for atoms are of the form

$$d_{i,n} + K_{i,w} \rho_i = 0; \quad K_{i,w} = \frac{2\gamma_{i,w}}{2 - \gamma_{i,w}} \sqrt{\frac{1}{2\pi} \frac{RT}{M_i}} \quad (3)$$

where $\gamma_{i,w}$ - the probability of heterogeneous recombination of the i -th chemical species.

In hypersonic flow a shock wave is formed around a body. Shock-capturing or shock-fitting approach is used. In the latter case the shock wave is seen as a flow boundary with the implementation on it of the Rankine-Hugoniot conditions, which result from integration of the Navier-Stokes equations (1) across the shock, neglecting the source term S and the derivatives along it. Assuming that a coordinate line $\eta = \text{const}$ coincides with the shock wave the Rankine-Hugoniot conditions can be represented in the form $\mathbf{F}_\infty = \mathbf{F}_s$ or in more details (for a perfect gas):

$$\begin{aligned} \rho_s (V_{ns} - D) &= \rho_\infty (V_{n\infty} - D) \\ \rho_s (V_{ns} - D)^2 + P_s &= \rho_\infty (V_{n\infty} - D)^2 + P_\infty \\ \rho_s (V_{ns} - D) V_{\tau s} &= \rho_\infty (V_{n\infty} - D) V_{\tau\infty} \\ h_s + \frac{(V_{ns} - D)^2}{2} + \frac{V_{\tau s}^2}{2} &= h_\infty + \frac{(V_{n\infty} - D)^2}{2} + \frac{V_{\tau\infty}^2}{2} \end{aligned} \quad (4)$$

here indices ∞ and s stand for parameters ahead and behind the shock, D - shock velocity, V_τ and V_n - projection of flow velocity on the directions of the tangent τ and the external normal \mathbf{n} to the shock wave. In (4) terms are omitted responsible for the processes of viscosity and thermal conductivity, because in the calculation results presented below the shock wave fitting is used for flows at high Reynolds numbers.

2.4 Numerical method

An implicit finite-difference numerical scheme linearized with respect to the previous time step τ_n for the Navier-Stokes equations (1) in general form can be written as follows:

$$\left[\mathbf{I} + \Delta\tau \left\{ \delta_\xi \mathbf{A} + \delta_\eta \mathbf{B} + \delta_\zeta \mathbf{C} - \mathbf{T} \right\} \right] \Delta\mathbf{Q} = -\Delta\tau \mathbf{R}^n \quad (5)$$

$$\mathbf{R}^n = \delta_\xi \mathbf{E} + \delta_\eta \mathbf{F} + \delta_\zeta \mathbf{G} - \mathbf{S}; \quad \mathbf{A} = (\partial \mathbf{E} / \partial \mathbf{Q})^n; \quad \mathbf{B} = (\partial \mathbf{F} / \partial \mathbf{Q})^n; \quad \mathbf{C} = (\partial \mathbf{G} / \partial \mathbf{Q})^n; \quad \mathbf{T} = (\partial \mathbf{S} / \partial \mathbf{Q})^n$$

Here symbols δ_ξ , δ_η and δ_ζ denote finite-difference operators which approximate the partial derivatives $\partial/\partial\xi$, $\partial/\partial\eta$ and $\partial/\partial\zeta$, the index n indicates that the value is taken at time τ_n , \mathbf{I} - identity matrix, $\Delta\mathbf{Q} = \mathbf{Q}^{n+1} - \mathbf{Q}^n$ - increment vector of the conservative variables at time-step $\Delta\tau = \tau_{n+1} - \tau_n$.

Let us consider first the inviscid flow. Yoon & Jameson (1987) have proposed a method of approximate factorization of the algebraic equations (5) - Lower-Upper Symmetric Successive OverRelaxation (LU-SSOR) scheme. Suppose that in the transformed coordinates (ξ, η, ζ) the grid is uniform and grid spacing in all directions is unity $\Delta\xi = \Delta\eta = \Delta\zeta = 1$. Then the LU-SSOR scheme at a point (i, j, k) of a finite-difference grid can be written as:

$$\mathbf{L}\mathbf{D}^{-1}\mathbf{U}\Delta\mathbf{Q} = -\mathbf{R}^n \quad (6)$$

$$\mathbf{L} = \mathbf{D} + \mathbf{L}^*, \quad \mathbf{U} = \mathbf{D} + \mathbf{U}^*, \quad \mathbf{D} = \left\{ \frac{1}{\Delta\tau} + \beta(\rho_A + \rho_B + \rho_C) \right\} \mathbf{I} - \mathbf{T}$$

$$\mathbf{L}^* = -\mathbf{A}_{i-1,j,k}^+ - \mathbf{B}_{i,j-1,k}^+ - \mathbf{C}_{i,j,k-1}^+, \quad \mathbf{U}^* = \mathbf{A}_{i+1,j,k}^- + \mathbf{B}_{i,j+1,k}^- + \mathbf{C}_{i,j,k+1}^-$$

where

$$\mathbf{A}^\pm = (\mathbf{A} \pm \beta\rho_A \mathbf{I}) / 2; \quad \rho_A = U + a\sqrt{\xi_x^2 + \xi_y^2 + \xi_z^2}$$

$$\mathbf{B}^\pm = (\mathbf{B} \pm \beta\rho_B \mathbf{I}) / 2; \quad \rho_B = V + a\sqrt{\eta_x^2 + \eta_y^2 + \eta_z^2}$$

$$\mathbf{C}^\pm = (\mathbf{C} \pm \beta\rho_C \mathbf{I}) / 2; \quad \rho_C = W + a\sqrt{\zeta_x^2 + \zeta_y^2 + \zeta_z^2}$$

Here the indices of the quantities at the point (i, j, k) are omitted for brevity, $\beta \geq 1$ is a constant, ρ_A , ρ_B , ρ_C - the spectral radii of the "inviscid" parts of the Jacobians \mathbf{A} , \mathbf{B} и \mathbf{C} , a - the speed of sound. Inversion of the equation system (6) is made in two steps:

$$\mathbf{L}\Delta\mathbf{Q}^* = -\mathbf{R}^n \quad (7a)$$

$$\mathbf{U}\Delta\mathbf{Q} = \mathbf{D}\Delta\mathbf{Q}^* \quad (7b)$$

It is seen from (6) that for non chemically reacting flows ($\mathbf{S}=0$, $\mathbf{T}=0$) LU-SSOR scheme does not require inversion of any matrices. For reacting flows due to the presence of the Jacobian of the chemical source $\mathbf{T} \neq 0$, the "forward" and "back" steps in (7) require, generally speaking, matrix inversion. However, calculations have shown that if the conditions are not too close to equilibrium then in the "chemical" Jacobian \mathbf{T} one can retain only diagonal terms which contain solely the partial derivatives with respect to concentrations of chemical species. In this approximation, scheme (6) leads to the scalar diagonal inversion also for the case of chemically reacting flows. Thus calculation time grows directly proportionally to the number of chemical species concentrations. This is important in calculations of complex flows of reacting gas mixtures, when the number of considered chemical species is large.

In the case of viscous flow, so as not to disrupt the diagonal structure of scheme (6), instead of the "viscous" Jacobians \mathbf{A}_v , \mathbf{B}_v и \mathbf{C}_v their spectral radii are used:

$$\rho_{Av} = \frac{\gamma}{Pr} \frac{\mu}{\rho} (\xi_x^2 + \xi_y^2 + \xi_z^2); \quad \rho_{Bv} = \frac{\gamma}{Pr} \frac{\mu}{\rho} (\eta_x^2 + \eta_y^2 + \eta_z^2); \quad \rho_{Cv} = \frac{\gamma}{Pr} \frac{\mu}{\rho} (\zeta_x^2 + \zeta_y^2 + \zeta_z^2)$$

In the finite-difference equation (6) central differences are employed, both for viscous and convective fluxes. The use of central differences to approximate the convective terms can cause non-physical oscillations of the flow parameters at high Reynolds numbers. To suppress such numerical oscillations artificial dissipation terms were added in the right part **R** of (6) according to Pulliam (1986). In calculations presented below it was assumed that the derivatives $\partial\xi/\partial t$, $\partial\eta/\partial t$ and $\partial\zeta/\partial t$ are zero and $\Delta\tau = \infty$. Since steady flow is considered, these assumptions do not affect the final result.

3. Calculation results

3.1 Flow and heat transfer on blunt delta wing

In thermovision experiments (Gubanova et al, 1992) in hypersonic flow past a delta wing with blunt nose and edges two regions of elevated heat were observed on its windward surface. At a distance of approximately 12-15 r from the nose of the wing (r – nose radius) there were narrow bands of high heat fluxes which extended almost parallel to the symmetry plane at a small interval (3-5 r) from it to the final section of the wing at $x \approx 100 r$ (see Fig. 1, in which the calculated distribution of heat fluxes is shown at the experimental conditions). The level of heat fluxes in the bands was approximately twice the value of background heat transfer corresponding to the level for a delta plate with sharp edges under the same conditions. It turned out that this effect exists in a fairly narrow range of flow parameters. In particular, on the same wing but with a sharp tip a similar increase in heat flux was not observed. This effect was explained by the interaction of shock waves arising at the tip and on the blunt edges of the wing (Gubanova et al, 1992; Lesin & Lunev, 1994). In this section numerical results calculated for the experimental conditions are presented and compared with measured heat flux values (see also (Vlasov et al., 2009)).

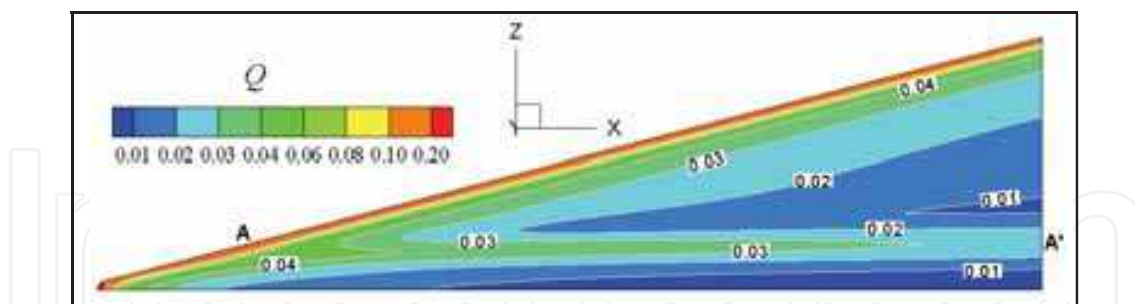


Fig. 1. Calculated distribution of non-dimensional heat flux $Q = q/q_0$ on the windward side of the blunt delta wing. q_0 – heat flux at the stagnation point of a sphere with a radius equal to the nose radius of the wing

Perfect gas hypersonic flow ($\gamma = 1.4$) past a delta wing with a spherical nose and cylindrical edges of the same radius is considered. Mach and Reynolds numbers calculated with free stream flow parameters and the wing nose radius are $M_\infty = 14$ and $Re_\infty = 1.4 \cdot 10^4$, angle of attack $\alpha = 10^\circ$, wing sweep angle $\lambda = 75^\circ$. The free stream stagnation temperature $T_{0\infty} = 1205$ K, the wall temperature $T_w = 300$ K. Due to the symmetry of flow, only half of the wing is computed. The flow calculation was performed with shock-fitting procedure, the computational grid is $120 \times 40 \times 119$ (in the longitudinal, transverse and circumferential

directions, respectively, see Fig. 2). Below in this section all quantities with a dimension of length, unless otherwise specified, are normalized to the wing nose radius r .

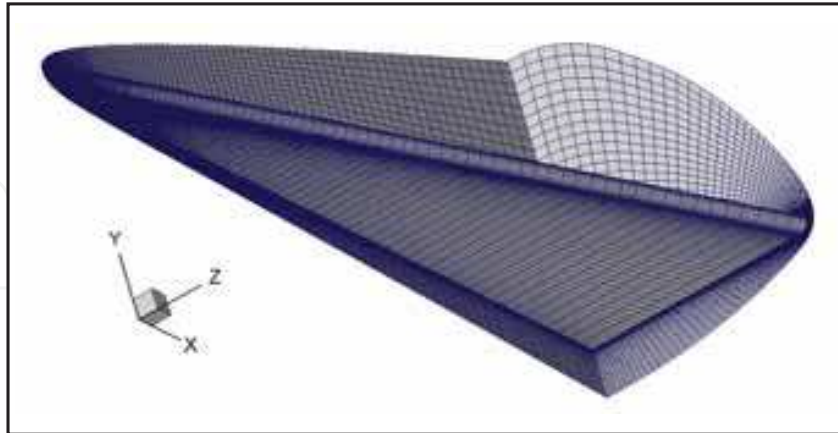


Fig. 2. The computational grid on the wing surface, in the plane of symmetry ($z = 0$) and in the exit section for the converged numerical solution

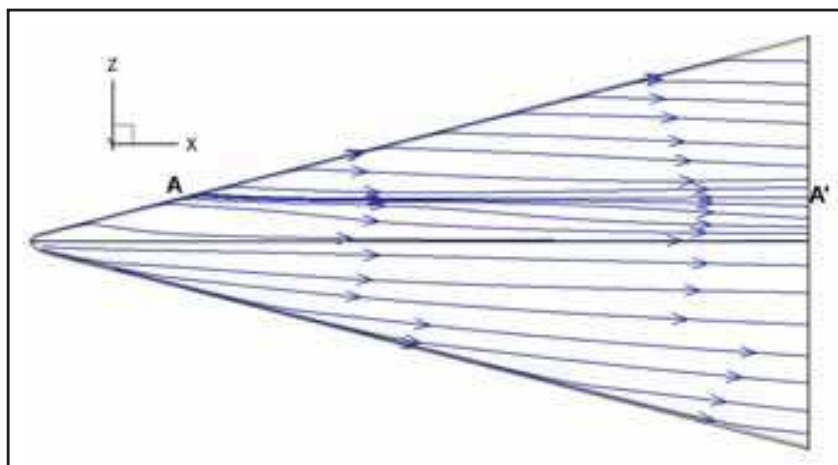


Fig. 3. Streamlines near the windward surface of the wing. Top – at a distance of one grid step from the wall, bottom – at the outer edge of the boundary layer

Calculated patterns of streamlines near the windward surface of the wing at a distance of one grid step from the wall and at the outer edge of the boundary layer are shown in Fig. 3. The streamlines, flowing down from the wing edge on the windward plane at almost constant pressure, form the line of diverging flow (line **A-A'**), along which there are bands of elevated heat fluxes. At the symmetry plane a line of converging streamlines is realized along the entire length of the wing, but upstream the shock interaction point **A** flow impinges on the symmetry plane from the edges, and downstream from **A** – from the diverging line **A-A'**. A characteristic feature of the considered case is that the distribution of heat fluxes on the windward side is mainly determined by the values of convergence and divergence of streamlines at almost constant pressure (see Fig. 4, which shows the distribution of pressure and heat flux on the windward side in several sections $x = \text{const}$). Local maxima of heat fluxes near symmetry plane appear only at $x > 15$ near the line $z = 4$ (after the nose shock wave intersects with the shock wave from the edges) and the relative intensity of these heat peaks grows with increasing distance from the nose (Fig. 4b).

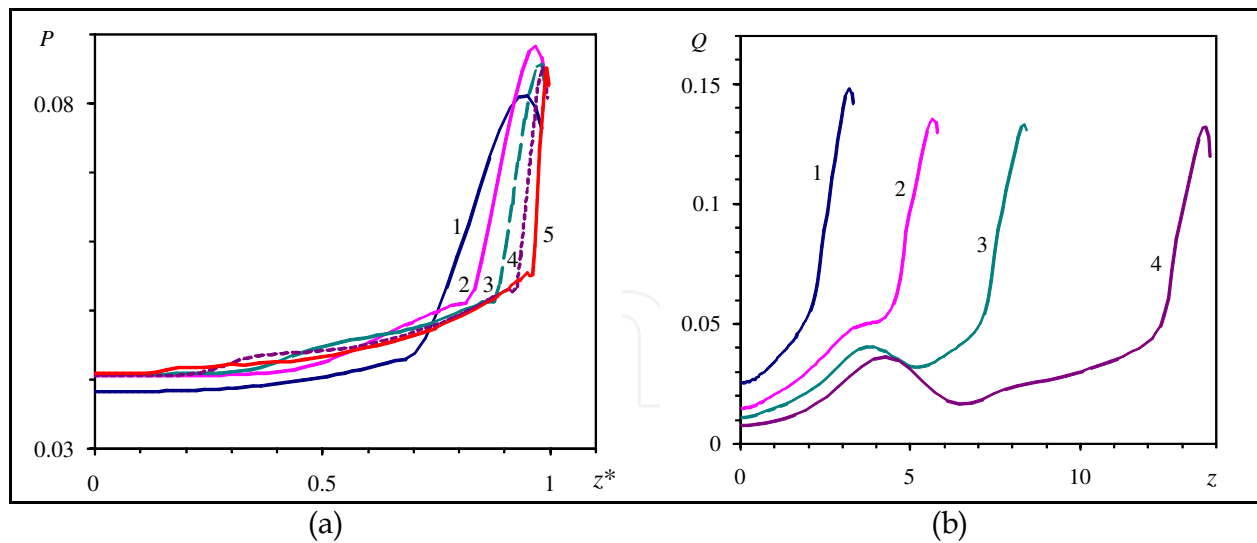


Fig. 4. Pressure distribution $P = p / \rho_\infty V_\infty^2$ (a) and heat flux $Q = q / q_0$ (b) on windward side of wing in sections: 1-5 - $x = 10, 20, 30, 50, 90$, $z^* = z / z_{max}$, z_{max} - wingspan in section $x = \text{const}$

Comparison of the upper and lower parts of Fig. 3 shows that the flow near the wall and at the outer edge of the boundary layer are noticeably different, the streamlines near the wall are directed to the symmetry plane (converging), and in inviscid region - from it (diverging). It follows that the velocity component directed along the wing chord changes sign across the boundary layer, which indicates the existence of transverse vortex (cross separation flow) in the boundary layer. This is illustrated in Fig. 5a, which shows the projection of streamlines on the plane of the cross section at $x = 90$.

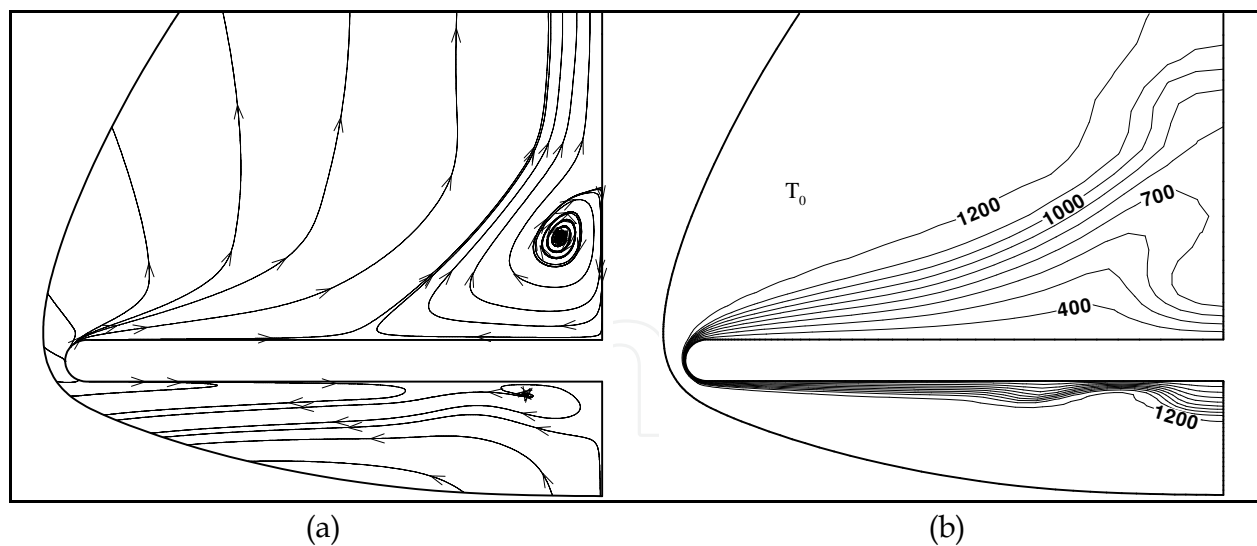


Fig. 5. Projection of streamlines (a) and isolines of stagnation temperature T_0 , K (b) in cross section $x = 90$

The distribution of the boundary layer thickness is clearly seen in Fig. 5b, which shows the contours of the stagnation temperature T_0 in the cross section $x = 90$. On the windward side of the wing minimum thickness of the boundary layer is located on the diverging line (line A-A' in Fig. 3). On the left and on the right sides of the diverging line there are converging lines with a thicker boundary layer (about 2 and 3 times respectively). One of the

converging lines is the symmetry plane. Here the boundary layer thickness on the windward side reaches a maximum, amounting to about one-third of the shock layer thickness.

Near the wing edge because of the expansion and acceleration of the flow the boundary layer thickness decreases sharply (at the edge it is almost 20 times less than at the symmetry plane on the windward side). On the leeward side of the wing flow separation occurs, and the concept of the boundary layer loses its meaning. Here scope of viscous flow is half the shock layer.

The shape of calculated shock wave in Fig. 6a, induced by the wing nose as a blunt body, is determined by the law of the explosive analogy, so that some front part of the wing $x \leq x_A \approx 15$ will be located inside the initially axisymmetric shock wave. The coordinate of point A (x_A) is located in the vicinity of interaction region of shock waves induced by the nose and the edges of the wing. Here the profiles of pressure and heat flux along the edge are local maxima.

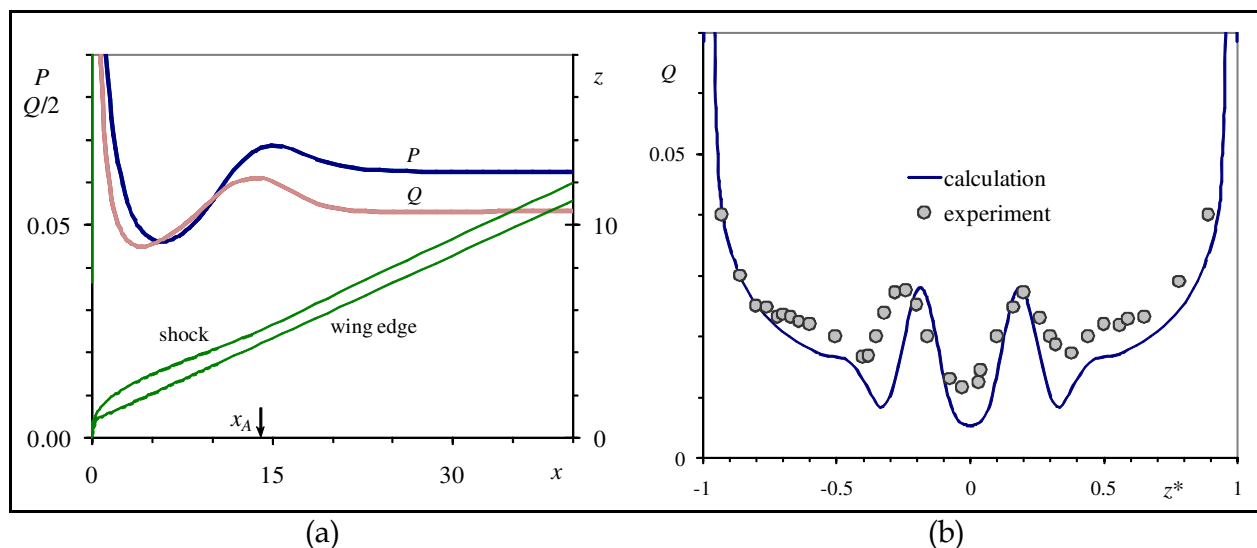


Fig. 6. Profiles of pressure, heat flux and the shock wave along the wing edge (a) and distribution of heat fluxes in cross section $x = 90$ (b)

In Fig. 6b the distribution of computed heat fluxes q/q_0 in the neighborhood of the wing end section at $x = 90$ is presented in comparison with the experiment of Gubanov et al. (1992) depending on the transverse coordinate z . On the whole the calculation correctly predicts the magnitude and position of local maximum of heat flux near the symmetry plane, taking into account the small asymmetry in the experimental data. Note that near the minima of heat fluxes calculated values are lower than experimental ones, probably due to effect of smoothing of experimental data in these narrow regions.

3.2 Heat transfer on test model of Pre-X space vehicle

Currently developed hypersonic aircraft have dimensions several times smaller than previously created space vehicles "Shuttle" and "Buran". This results in increase of heat load on a vehicle during flight, and therefore the problem of reliable calculation of heat fluxes on the surface for such relatively small bodies is particularly important. Thus the problem arises of verification of the employed physical models and numerical methods by comparing calculation results with experimental data.

In 2006-2007 on TsNIImash's experimental base in a piston gasdynamic wind tunnel PGU-7 a heat transfer study has been conducted on a small-scale model of Pre-X reentry demonstrator (Baiocco, 2006). This vehicle is designed to obtain in flight conditions experimental data pertaining to aerothermodynamic phenomena that are not modeled in ground tests, but they are critical for design of a vehicle returning from the Earth's orbit. In particular, Pre-X demonstrator is developed to test in a real flight and in specified locations on the vehicle surface samples of reusable thermal protection materials and to assess their durability.

During the study thermovision measurements have been conducted of heat fluxes on the model of scale 1/15 at various flow regimes - $M = 10$, $Re = 1 \cdot 10^6 - 5 \cdot 10^6$ 1/m (Kovalev et al., 2009). Processing of thermovision measurements was carried out in accordance with standard technique and composed of determination of the model surface temperature during experiment, extraction from these data distributions of heat fluxes on the observed model surface and binding of the resulting thermovision frame to a three-dimensional CAD model of the demonstrator. The same CAD model has been used for numerical simulation of heat transfer on the Pre-X test model.

As a normalizing value the heat flux q_0 at the stagnation point of a sphere with radius of 70 mm is adopted, which is determined using the Fay-Riddell formula. Advantage of data presentation in this form is due to invariability of the relative values $Q = q/q_0$ on most model surface at variations of flow parameters.

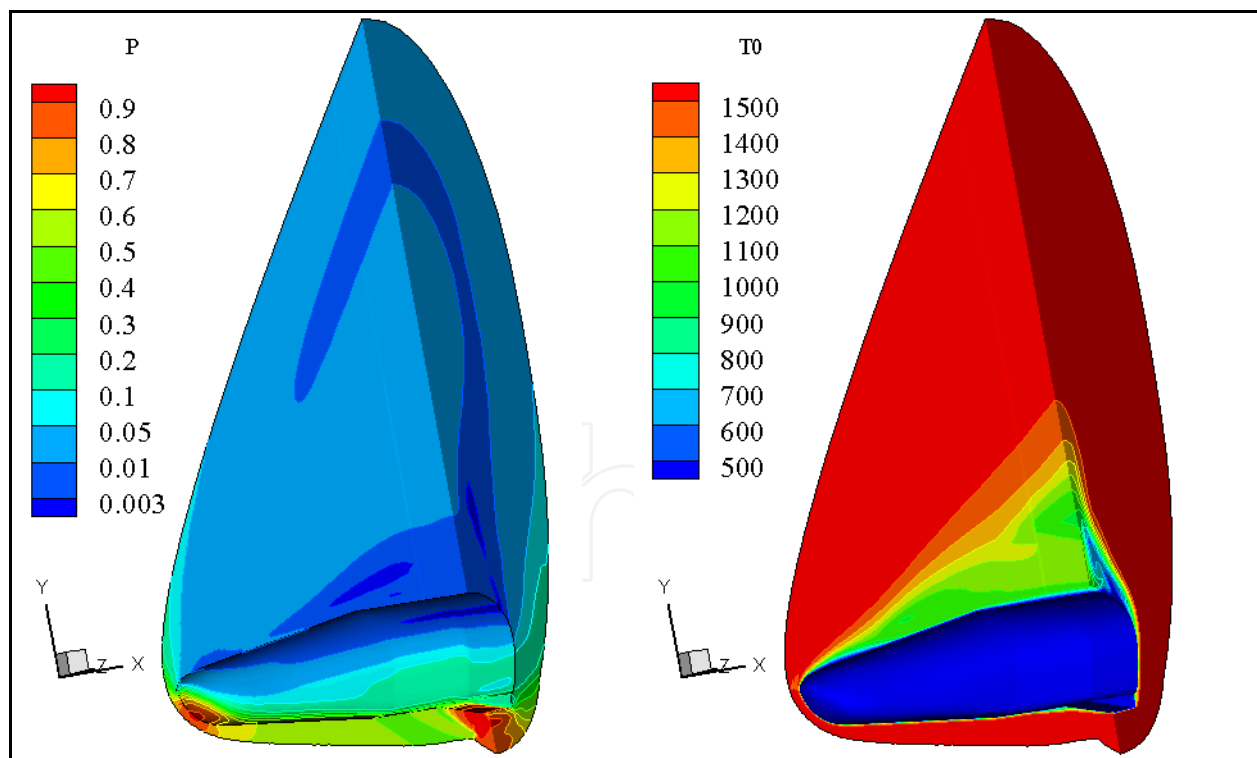


Fig. 7. Calculated distributions of pressure $P = p/\rho_\infty V_\infty^2$ (left) and stagnation temperature T_0 , K (right) on surface and in shock layer (in symmetry plane and in exit section) for test model of Pre-X vehicle

On the base of the numerical solution of the Navier-Stokes equations a study was carried out of flow parameters and heat transfer for laminar flow over a test model of Pre-X space

vehicle for experimental conditions in the piston gasdynamic wind tunnel. Mach and Reynolds numbers, calculated from the free-stream parameters and the length of the model (330 mm), are $M_\infty = 10$ and $Re_\infty = 7 \cdot 10^5$. Angle of attack - 45° . The flap deflection angle was (as in the experiment) $\delta = 5, 10$ and 15° . The stagnation temperature of the free-stream flow and the wing surface temperature - $T_{0\infty} = 1000$ K and $T_w = 300$ K, respectively. An approximation of a perfect gas was used with ratio of specific heats $\gamma = 1.4$. The calculations were performed with a shock-fitting procedure, i.e. the bow shock was considered as a discontinuity with implementation of the Rankine-Hugoniot relations (4) across it. On the model surface no-slip and fixed temperature conditions were set. Note that in view of the flow symmetry computations were made only for a half of the model, although in the figures below for comparison with experiment the calculated data (upon reflection in the symmetry plane) are presented on the entire model.

The overall flow pattern obtained in the calculations over the test model of Pre-X space vehicle is shown in Fig. 7, where for the case of the flap deflection angle $\delta = 15^\circ$ pressure and stagnation temperature T_0 isolines in the shock layer and on the model surface are shown. It is seen that there are two areas of high pressure: on the nose tip of the model ($P \approx 0.92$) and on the deflection flaps. In the latter case the pressure in the flow passing through the two shock waves reaches $P \approx 1.3$. Isolines of T_0 show the size of regions where viscous forces are significant: a thin boundary layer on the windward side of the model and an extensive separation zone on the leeward side. The small separation zone, appearing at deflection flaps, although about four times thicker than the boundary layer upstream of it is almost not visible in the scale of the figure.

Fig. 8 shows the distributions of relative heat flow Q on the windward side of the model obtained in the experiments and in the calculations at deflection angles of flaps $\delta = 5, 10$ and 15° . For the case $\delta = 5^\circ$ it can be noted rather good agreement between experiment and calculation in the values of heat flux in the central part of the model and on the flaps. It is evident that before deflected flaps there is a region of low heat fluxes caused by near separation state (according to calculation results) of the boundary layer.

In analyzing the experimental data it should be taken into account the effect of "apparent" temperature reduction of the surface area with a large angle to the thermovision observation line. It is precisely this effect that explains the fact that in the nose part of the model the experimental values of heat flux are less than the calculated ones. Also narrow zones of high (at the sharp edges of the flaps) or low (in the separation zone at the root of the flaps) values of heat flux are smoothed or not visible in the experiment due to insufficient resolution of thermovision equipment. The resolution capability of thermovisor is clearly visible by the size of cells in the experimental isoline pattern of heat flux in Fig. 8. It should be noted that the calculations do not take into account a slit between the deflection flaps available on the test model, the presence of which should lead to a decrease in the separation region in front of the flaps.

At an angle of flap deflection $\delta = 10^\circ$, as in the previous case $\delta = 5^\circ$, there is fairly good agreement between calculation and experiment for the values of heat flux in the central part of the model and on the flaps. The calculations show that the growth of the flap deflection angle δ from 5° to 10° results in the formation of a large separation zone in front of the flaps and in a decrease in heat flux value Q from 0.2 to 0.1.

At the largest angle of flap deflection $\delta = 15^\circ$ the maximum of calculated heat flux occurs in the zone of impingement of the separated boundary layer, where the level of Q is 2-3 times higher than its level on the undeflected flap. The coincidence of calculation results with

experimental data in the front part of the model up to the separation zone before the flaps is satisfactory. On the flaps the level of heat flux in the experiment is about one and a half times more than in the calculation. This difference in heat flux values is apparently due to laminar-turbulent transition in separation region induced by the deflected flaps which takes place in the experiment.

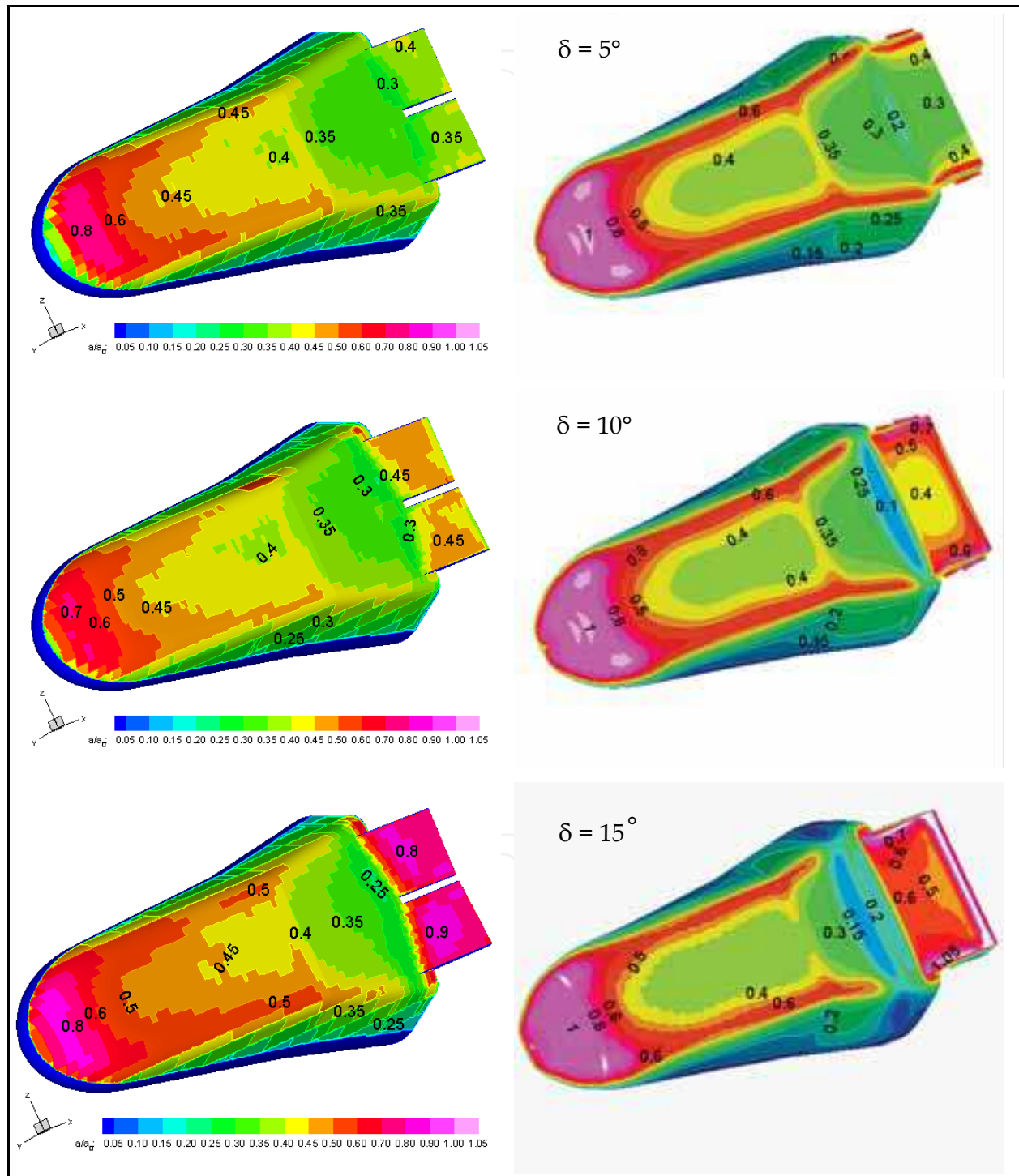


Fig. 8. Experimental (left) and calculated (right) heat fluxes $Q = q/q_0$ on windward side of test model of Pre-X space vehicle at different deflection angles of flaps δ .

3.3 Flow and heat transfer on a winged space vehicle at reentry to Earth's atmosphere

This section presents the results of numerical simulation of flow and heat transfer on a winged version of the small-scale reentry vehicle, being developed in TsAGI (Vaganov et al, 2006), moving at hypersonic speed in the Earth's atmosphere. Calculations were made using two physical-chemical models of the gas medium - equilibrium and non-equilibrium chemically reacting air.

The bow shock was captured in contrast to the previous two flow cases. Thus on the inflow boundary the free-stream conditions were specified. On the vehicle surface no-slip and adiabatic wall conditions were supposed. In calculations with use of the nonequilibrium air model the vehicle surface was supposed to be low catalytical with the probability of heterogeneous recombination of O and N atoms equal to $\gamma_A = 0.01$.

A computational grid was provided by Mikhailin V.A. (Dmitriev et al., 2007), and was taken from the inviscid flow calculation. The number of points in the direction normal to the vehicle surface has been increased to resolve the wall boundary layer. Part of the results presented below was reported in (Dmitriev et al., 2007; Gorshkov et al., 2008a).

Calculations were performed for two points of a reentry trajectory, for which thermal loads are close to maximum (Table 1). The angle of attack $\alpha = 35^\circ$, the vehicle length $L = 9\text{m}$. A grid $93 \times 50 \times 101$ in the longitudinal, transverse and circumferential directions respectively were used in the calculations. The surface grid of the vehicle is shown in Fig. 9.

H , km	V_∞ , m/sec	$Re_{\infty,L}$	M_∞	P_∞ , atm	T_∞ , K
70	5952	$3.46 \cdot 10^5$	20.0	$5.76 \cdot 10^{-5}$	219
63	5152	$6.84 \cdot 10^5$	16.6	$1.59 \cdot 10^{-4}$	243

Table 1. Parameters of trajectory points

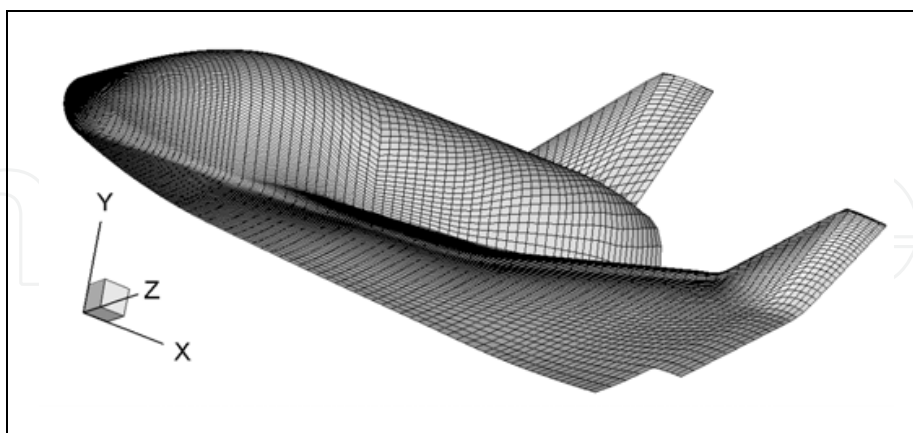


Fig. 9. Surface grid of the small-scale reentry vehicle

In Fig. 10a contours of total enthalpy H_0 on the surface and in the shock layer near the reentry vehicle are shown. On the windward side one can see the shock wave, the thin wall boundary layer and the inviscid flow between them, in which the values of H_0 are constant. In the calculations the shock wave is smeared upon 3-5 grid points and has a finite thickness due to the use of artificial dissipation. In particular, a local decrease in H_0 in a strong shock

wave on the windward side, which can be seen in the figure, has no physical meaning and is due to the influence of artificial dissipation. Recall that the Navier-Stokes equations do not correctly describe the shock structure at Mach numbers $M > 1.5$.

In the shock layer on the leeward side it is visible a large area with reduced values of total enthalpy $H_0 < H_{0\infty}$ ($H_{0\infty}$ - total enthalpy in the free-stream), which arises as a result of boundary layer separation from the vehicle surface.

Chemical processes occurring in the shock layer over the vehicle are illustrated in Fig. 10b, which shows contours of mass concentrations of oxygen atoms c_o . Under the considered conditions in the vicinity of the vehicle nose behind the shock wave O_2 dissociation is complete. On the windward side downstream the nose in the shock layer and on the surface the recombination occurs and the concentration of O decreases. In contrast, on the leeward side where the flow is very rarefied, the level of c_o remains high, indicating that the process of recombination of atomic oxygen is frozen.

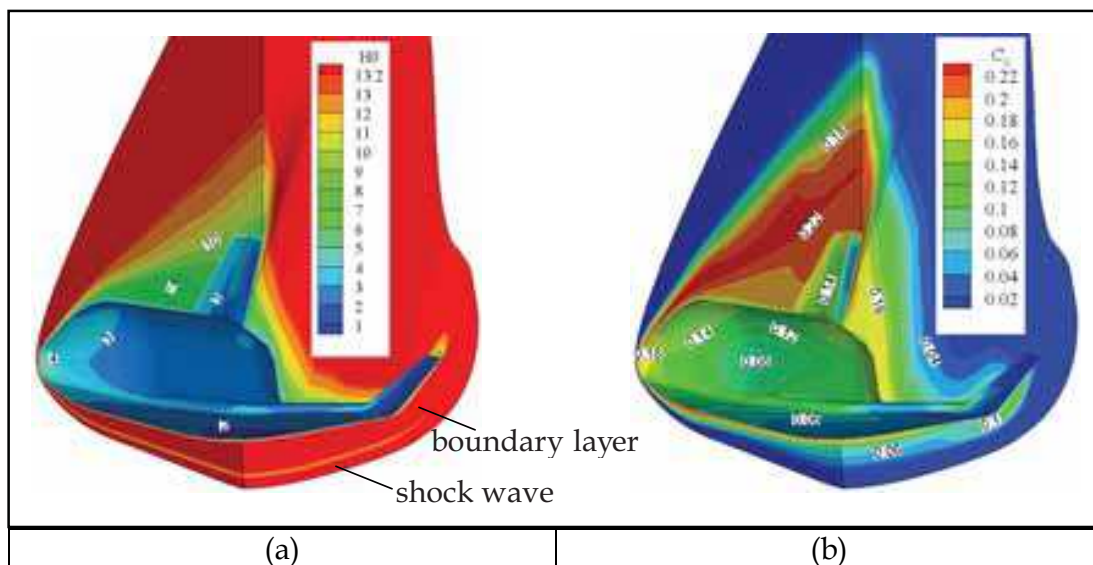


Fig. 10. Total enthalpy, MJ/kg (a), and mass concentration of oxygen atoms (b) on the surface and in the shock layer near the vehicle. $H = 63$ km

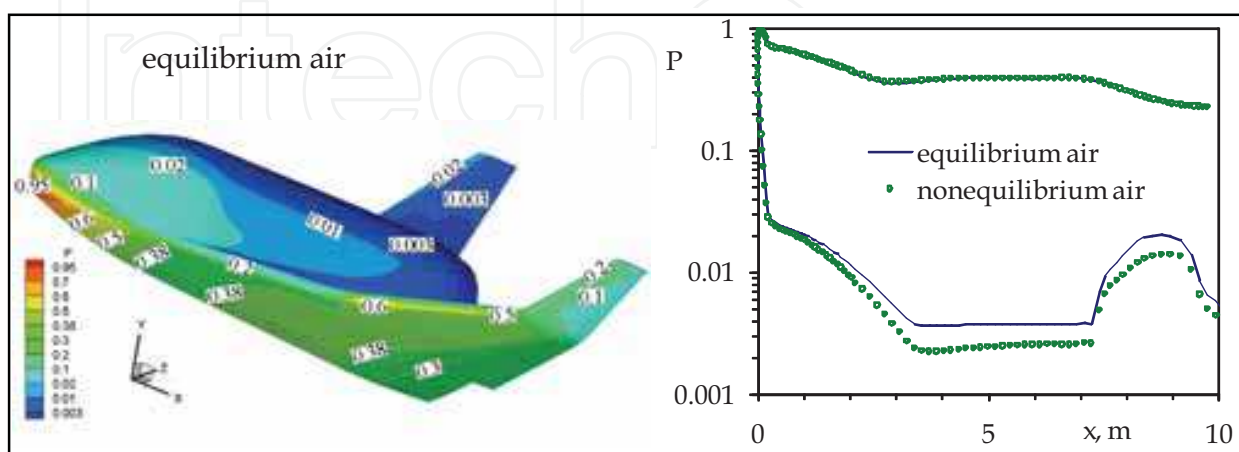


Fig. 11. Pressure distribution $P = p/\rho_{\infty}V_{\infty}^2$ on vehicle surface, overall view (left) and in symmetry plane (right), $H = 63$ km

In Fig. 11 and 12 isolines of pressure, heat flux q_w and equilibrium radiation temperature T_w on the vehicle surface are shown for cases of equilibrium and non-equilibrium dissociating air. Comparison of q_w and T_w distributions on the vehicle surface in the symmetry plane for two air models are depicted in Fig. 13.

Analysis of the calculation results shows that pressure distribution on the windward surface of the vehicle does not depend on physical-chemical model of the gas medium - the difference in pressure values for equilibrium and non-equilibrium air flow is 1 - 2%. On the leeward side pressure on the surface for nonequilibrium flow may be nearly two times lower than for equilibrium flow (e.g., in the vicinity of the tail). This is probably due to the fact that the effective ratio of specific heats for nonequilibrium air is greater than for equilibrium air, because in the shock layer on the leeward side nonequilibrium flow is chemically frozen, and here there is a sufficiently high concentration of atoms (see Fig. 10b).

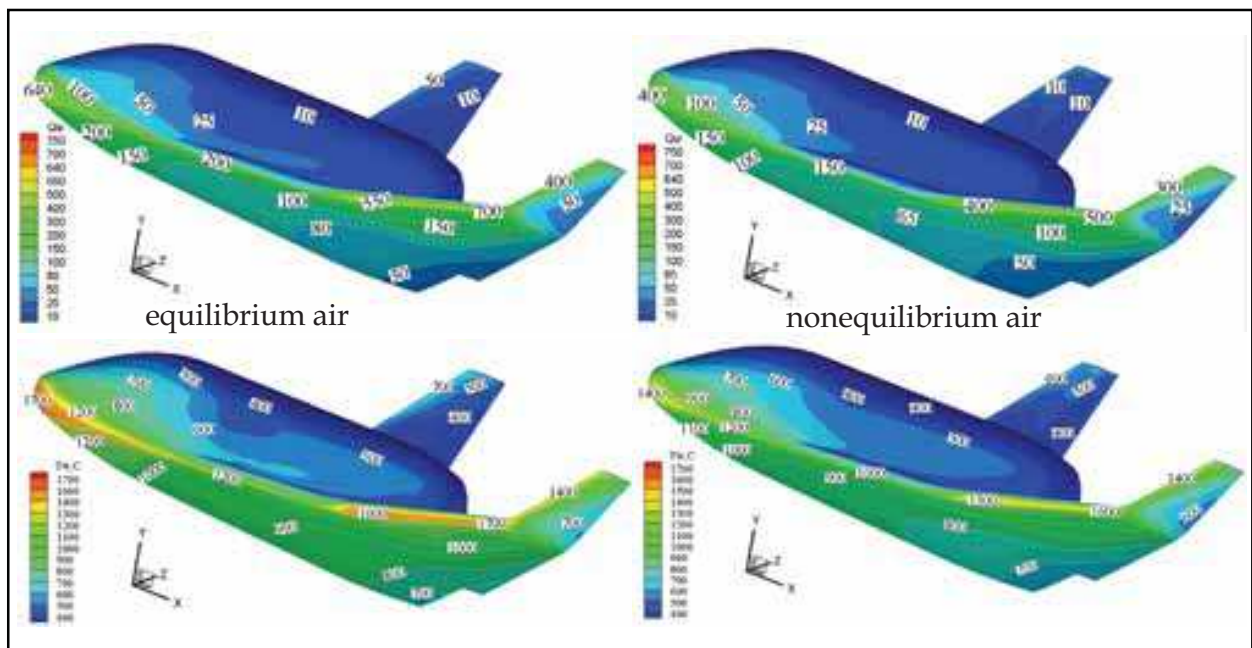


Fig. 12. Distributions of heat flux q_w , kW/m², (top) and equilibrium radiation temperature T_w , °C, (bottom) on the vehicle surface, $H = 63$ km

Nonequilibrium chemical processes in the shock layer and finite catalytic activity of the vehicle surface ($\gamma_A = 0.01$) significantly reduce the calculated levels of heat transfer in comparison with the case of equilibrium air flow. The most significant decrease in heat flux is observed on the vehicle nose part (for $x \leq 1$ m) and in the vicinity of the tail. For example, at the nose stagnation point the level of heat flux decreases by about 40% - from 640 to 385 kW/m², while the surface temperature decreases by nearly 15% - from 1670 to 1430 °C.

Note a high heat flux level on the thin edge of the wing compared with one at the nose stagnation point. Particularly intense heating occurs at the sharp bend of the wing where the values of heat flux and surface temperature even slightly exceed their values at the front stagnation point. In the case of equilibrium air flow the exceeding for heat flux is about 10% (710 and 640 kW/m²), for temperature - 3% (1720 and 1670 °C). In the case of nonequilibrium air flow the exceeding is more significant, for heat flux - 30% (540 and 385 kW/m²), for temperature - 10% (1570 and 1430 °C).

In other parts of the vehicle surface difference in heat flux levels for the two air models is somewhat less, and it decreases downstream, presumably due to gradual recombination of atoms in the boundary layer at flowing along the surface in case of non-equilibrium air.

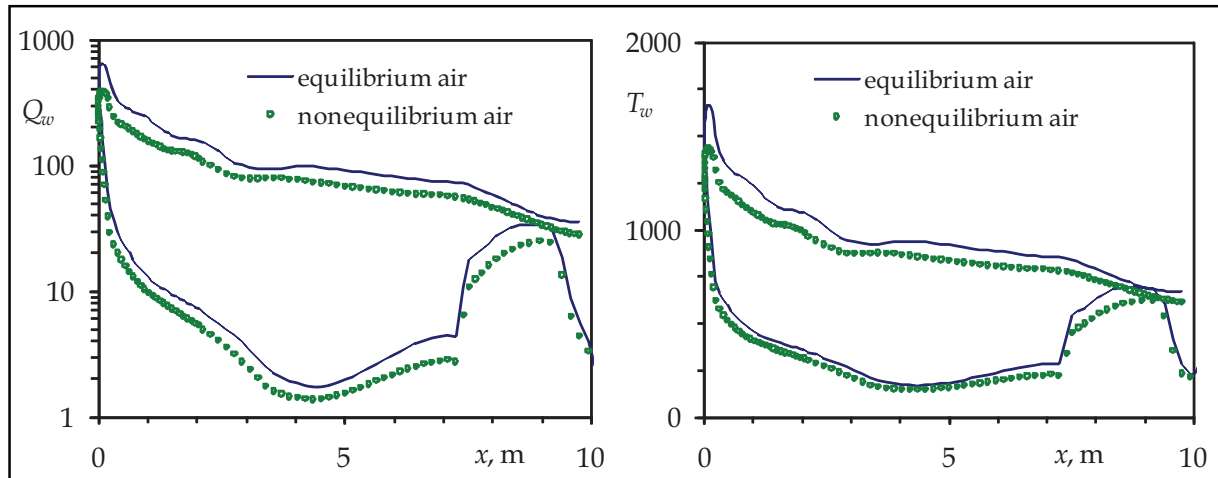


Fig. 13. Profiles of heat flux q_w , kW/m², (left) and equilibrium radiation temperature T_w , °C, (right) on vehicle surface in symmetry plane, $H = 63$ km

A similar flow and heat flux patterns are observed for the altitude $H = 70$ km, as seen in Fig. 14 where contours of heat flux and equilibrium radiation wall temperature are shown at this altitude for the two air models. For equilibrium air overall level of heat flux at 70 km is slightly higher than at 63 km. For example heat flux value at the nose stagnation point is increased by 5% (675 compared with 640 kW/m²). The opposite situation occurs for the model of nonequilibrium air, in this case the stagnation point heat flux value at 70 km is lower than at 63 km – by 7% (360 and 385 kW/m² respectively).

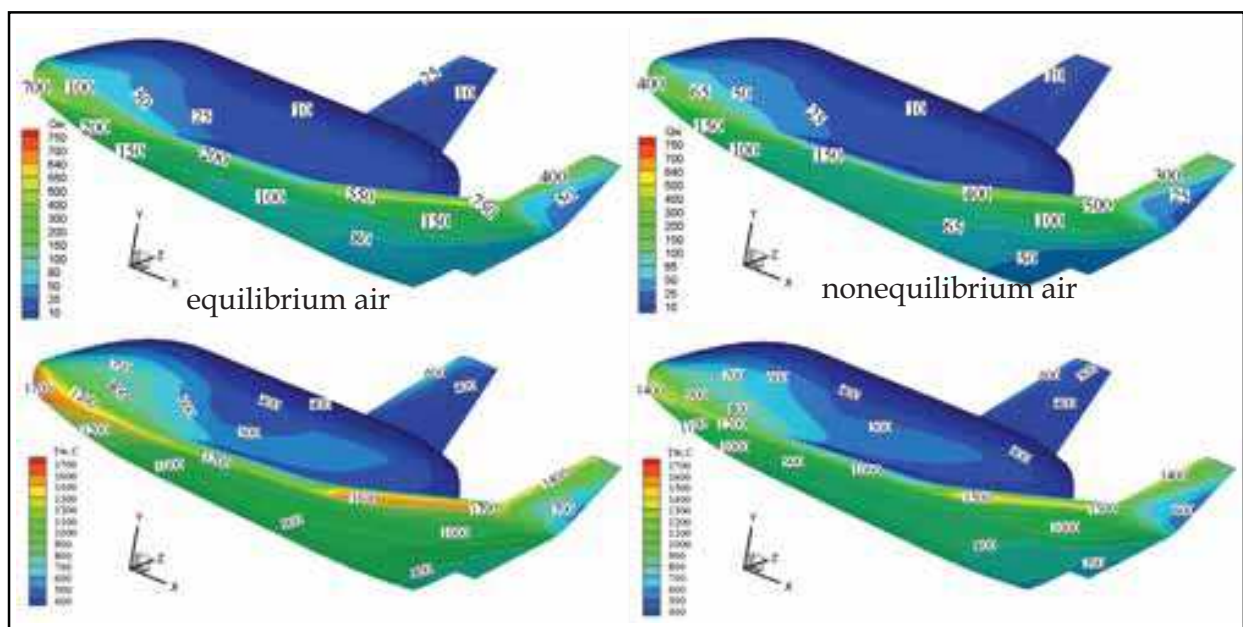


Fig. 14. Distributions of heat flux q_w , kW/m², (top) and equilibrium radiation temperature T_w , °C, (bottom) on the vehicle surface, $H = 70$ km

4. Conclusion

A three-dimensional stationary Navier–Stokes computer code for laminar flow, developed by the author, has been briefly described. The code is mainly intended to calculate super- and hypersonic flows over bodies accounting for high temperature real gas effects with special emphasis on convective heat transfer. Three gas models: perfect gas, equilibrium and nonequilibrium gas mixture can be used in the calculations.

In the chapter a comparison of code calculation results with experimental data is made for two perfect gas hypersonic flow cases at wind tunnel conditions. First case is a simulation of an anomalous heat transfer on the windward side a delta wing with blunt edges. On the whole the calculation correctly predicts the magnitude and position of local maximum of heat flux near the wing symmetry plane, taking into account a small asymmetry in the experimental data. Second case is a computation of heat transfer on a test model of the Pre-X demonstrator. Satisfactory agreement with thermovision heat fluxes on the smooth windward side and on the flaps is obtained, except for the largest deflection angle of flaps $\delta = 15^\circ$ when the level of heat flux in the experiment is about one and a half times more than in the calculation. This discrepancy is apparently due to laminar-turbulent transition in separation region induced by the deflected flaps which takes place in the experiment.

Third flow case concerns chemically reacting air flow at equilibrium or nonequilibrium conditions. Flowfield and convective heat transfer parameters for a winged shape of a small-scale reentry vehicle are calculated for two points of a reentry trajectory in the Earth's atmosphere. Heat flux and equilibrium radiation temperature distributions on the vehicle surface are obtained. Also regions of maximal thermal loadings are localized.

Calculations show that for nonequilibrium air flow the use of a low catalytic coating (with probability of heterogeneous recombination of atoms $\gamma_A = 0.01$) on the vehicle surface enables to decrease considerably the level of heat fluxes in regions of maximal heat transfer in the nose part and on the wing edges in comparison with equilibrium air flow. For example for trajectory points with maximal thermal load a reduction of up to 40% in heat flux (which results in a 15% reduction of equilibrium radiation wall temperature) can be obtained at the vehicle nose.

5. Acknowledgments

The author is grateful to Kovalev R.V., Marinin V.P. and Vlasov V.I. for delivering thermovision data on test model of Pre-X vehicle, and also to Churakov D.A. and Mihalina V.A. for providing computational grids.

6. References

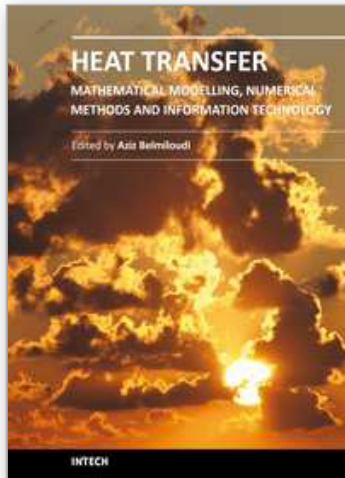
- Baiocco, P.; Guedron, S.; Plotard, P. & Moulin, J. (2006). The Pre-X atmospheric re-entry experimental lifting body: Program status and system synthesis, *Proceedings of 57th International Astronautical Congress*, 2-6 October 2006. IAC-06-D2.P.2.2
- Churakov, D.A.; Gorshkov, A.B.; Kovalev, R.V.; Vlasov, V.I.; Beloshitsky, A.V.; Dyadkin, A.A. & Zhurin, S.V. (2008). Heat Transfer of Reentry Vehicles during Atmosphere Flight, *Proceedings of 6-th European Symposium on Aerothermodynamics for Space Vehicles*, Versailles, France, 3 - 6 November 2008.

- Dmitriev, V.G.; Vaganov, A.V.; Gorshkov, A.B.; Lapygin, V.I.; Galaktionov, A.Yu. & Mikhailin, V.A. (2007). Analysis of Aerothermodynamic Parameters of Reusable Space Wing Vehicle, *Proceedings of 2nd European Conference for Aero-Space Sciences*, Brussels, Belgium, July 1-6 2007
- Gorshkov A.B. (1997) Calculation of Base Heat Transfer Behind Thin Cone-Shaped Bodies. *Cosmonautics and Rocket Engineering*, No. 11, (1997) pp. 13-20 (in Russian)
- Gorshkov, A.B.; Kovalev, R. V.; Vlasov, V. I. & Zemlyanskiy, B. A. (2008a). Simulation of Heat Transfer to Space Vehicles during a Gliding Reentry into Earth's Atmosphere, *Proceedings of 14th International Conference on Methods of Aerophysical Research (ICMAR-2008)*, Novosibirsk, Russia, 30 June - 06 July 2008
- Gorshkov, A.B.; Kovalev, R. V.; Vlasov & V. I., Zemlyanskiy, B. A. (2008b). Heat Transfer Investigation for Hypersonic Flow over Experimental Model of Pre-X Reentry Vehicle, *Proceedings of 7th Sino-Russian High-Speed Flow Conference (SRHFC-7)*, Novosibirsk, Russia, 1 - 3 July 2008
- Grantham W.L. (1970). Flight results of a 25,000 fps re-entry experiment, *NASA TN D 6062*.
- Gubanova, O.I.; Zemlyansky, B.A.; Lessin, A.B.; Lunev, V.V.; Nikulin, A.N. & Syusin A.V. (1992). Anomalous heat transfer on the windward side of a delta wing with a blunt tip in hypersonic flow, In: *Aerothermodynamics of aerospace systems*, Pt. 1, pp. 188-196, Moscow, TsAGI (in Russian)
- Hoffmann, K.A.; Chiang, S.T. (2000). *Computational fluid dynamics*, Vol. 2, Engineering Educational Systems, ISBN 0-9623731-3-3, Kansas, USA
- Inouye, Y. (1995). OREX flight - quick report and lessons learned. *Proceedings of 2nd European Symposium on Aerothermodynamics for Space Vehicles*, pp. 271-279, ESTEC, Noordwijk, The Netherlands, Europe Space Agency (November 1994).
- Kovalev, R.V.; Kislykh, V.V.; Kolozeznii, A.E.; Kudryavtsev, V.V.; Marinin, V.P.; Vlasov, V.I. & Zemliansky, B.A. (2009). Experimental studies of Pre-X vehicle heat transfer in PGU-7 test facility, *3rd European Conference for Aerospace Sciences (EUCASS-2009)*, Versailles, France, 6-9 July 2009
- Lesin, A.B. & Lunev, V.V. (1994). Heat transfer peaks on a blunt-nosed triangular plate in hypersonic flow. *Fluid Dynamics*, Vol. 29, No. 2, (April 1994) pp. 258-262, ISSN: 0015-4628
- Mason, E.A. & Saxena, S.C. (1958). Approximate Formula for the Thermal Conductivity of Gas Mixtures. *Phys. Fluids*, Vol. 1, No. 5, (1958) pp. 361-369
- Pulliam, T.H. (1986). Artificial dissipation models for the Euler equations. *AIAA Journal*, Vol.24, No. 12, (December 1986) pp. 1931-1940, ISSN: 0001-1452
- Vaganov, A.V.; Dmitriev, V.G.; Zadonsky, S.M.; Kireev, A.Y.; Skuratov, A.S. & Stepanov, E.A. (2006). Estimations of low-sized winged reentry vehicle heat regimes on the stage of its designing. *Physico-chemical kinetics in gas dynamics*, www.chemphys.edu.ru/pdf/2006-11-20-002.pdf (in Russian)
- Vlasov, V.I.; Gorshkov, A.B.; Kovalev, R.V. & Plastinin, Yu.A. (1997). Theoretical studies of air ionization and NO vibrational excitation in low density hypersonic flow around re-entry bodies. *AIAA Paper*. No. 97-2582 (1997)
- Vlasov, V. I. & Gorshkov, A. B. (2001). Comparison of the Calculated Results for Hypersonic Flow Past Blunt Bodies with the OREX Flight Test Data. *Fluid Dynamics*, Vol. 36, No 5, (October 2001) pp. 812-819, ISSN: 0015-4628

- Vlasov, V.I.; Gorshkov, A.B.; Kovalev, R.V. & Lunev, V.V. (2009). Thin triangular blunt-nosed plate in a viscous hypersonic flow. *Fluid Dynamics*, Vol. 44, No. 4 (August 2009) pp. 596-605, ISSN: 0015-4628
- Wilke, C. (1950). A Viscosity Equation for Gas Mixtures. *J.Chem.Phys.*, Vol. 18, No. 4, (1950) pp.517-519
- Yoon, S. & Jameson, A. (1987). An LU-SSOR Scheme for the Euler and Navier-Stokes Equations. *AIAA Paper*. No. 87-0600 (1987)

IntechOpen

IntechOpen



Heat Transfer - Mathematical Modelling, Numerical Methods and Information Technology

Edited by Prof. Aziz Belmiloudi

ISBN 978-953-307-550-1

Hard cover, 642 pages

Publisher InTech

Published online 14, February, 2011

Published in print edition February, 2011

Over the past few decades there has been a prolific increase in research and development in area of heat transfer, heat exchangers and their associated technologies. This book is a collection of current research in the above mentioned areas and describes modelling, numerical methods, simulation and information technology with modern ideas and methods to analyse and enhance heat transfer for single and multiphase systems. The topics considered include various basic concepts of heat transfer, the fundamental modes of heat transfer (namely conduction, convection and radiation), thermophysical properties, computational methodologies, control, stabilization and optimization problems, condensation, boiling and freezing, with many real-world problems and important modern applications. The book is divided in four sections : "Inverse, Stabilization and Optimization Problems", "Numerical Methods and Calculations", "Heat Transfer in Mini/Micro Systems", "Energy Transfer and Solid Materials", and each section discusses various issues, methods and applications in accordance with the subjects. The combination of fundamental approach with many important practical applications of current interest will make this book of interest to researchers, scientists, engineers and graduate students in many disciplines, who make use of mathematical modelling, inverse problems, implementation of recently developed numerical methods in this multidisciplinary field as well as to experimental and theoretical researchers in the field of heat and mass transfer.

How to reference

In order to correctly reference this scholarly work, feel free to copy and paste the following:

Andrey B. Gorshkov (2011). Aerodynamic Heating at Hypersonic Speed, Heat Transfer - Mathematical Modelling, Numerical Methods and Information Technology, Prof. Aziz Belmiloudi (Ed.), ISBN: 978-953-307-550-1, InTech, Available from: <http://www.intechopen.com/books/heat-transfer-mathematical-modelling-numerical-methods-and-information-technology/aerodynamic-heating-at-hypersonic-speed>

INTECH
open science | open minds

InTech Europe

University Campus STeP Ri
Slavka Krautzeka 83/A
51000 Rijeka, Croatia
Phone: +385 (51) 770 447
Fax: +385 (51) 686 166

InTech China

Unit 405, Office Block, Hotel Equatorial Shanghai
No.65, Yan An Road (West), Shanghai, 200040, China
中国上海市延安西路65号上海国际贵都大饭店办公楼405单元
Phone: +86-21-62489820
Fax: +86-21-62489821

www.intechopen.com

www.intechopen.com

IntechOpen

IntechOpen

© 2011 The Author(s). Licensee IntechOpen. This chapter is distributed under the terms of the [Creative Commons Attribution-NonCommercial-ShareAlike-3.0 License](#), which permits use, distribution and reproduction for non-commercial purposes, provided the original is properly cited and derivative works building on this content are distributed under the same license.

IntechOpen

IntechOpen